

## Restoration of interferometric images

### IV. An algorithm for super-resolution of stellar systems

B. Anconelli<sup>1</sup>, M. Bertero<sup>1</sup>, P. Boccacci<sup>1</sup>, and M. Carillet<sup>2</sup>

<sup>1</sup> INFN and DISI, Università di Genova, via Dodecaneso 35, 16146 Genova, Italy  
e-mail: bertero@disi.unige.it

<sup>2</sup> Laboratoire Universitaire d'Astrophysique de Nice, UMR 6525, Parc Valrose, 06108 Nice Cedex 02, France

Received 2 March 2004 / Accepted 13 October 2004

**Abstract.** In the framework of the methods we introduced for the restoration of images of Fizeau interferometers such as the Large Binocular Telescope, we propose an algorithm which is able to super-resolve compact stellar objects such as a binary system with an angular separation smaller than the angular resolution of the telescope. The method, which works also in the case of a monolithic mirror, is based on a simple modification of the Richardson-Lucy (RL) method or of the Ordered Subsets – Expectation Maximization (OS-EM) method for image deconvolution. In general, it consists of three steps: the first one requires a large number of RL-iterations, which are used to identify and estimate the domain of the unresolved object; the second one is a RL-restoration initialized with the mask of the domain. These two steps can provide a super-resolved image of the stellar system but the photometry of the stars may not be correct. Therefore their positions are derived from the result of the first two steps while their magnitudes are estimated in a third step by solving a simple least-squares problem. In order to show that the method can work in practice, we use (simulated) adaptive-optics-corrected point spread functions (PSF), both in the case of a monolithic and in the case of a binocular telescope, and we investigate mainly the case of binary systems. We analyze the limitations of the method in evaluating the angular separation and the relative magnitude of the two stars. The results we obtain are quite promising.

**Key words.** techniques: image processing – methods: data analysis – methods: numerical – techniques: high angular resolution

#### 1. Introduction

In two previous papers (Correia et al. 2002; Carillet et al. 2002) we present the Software Package AIRY (Astronomical Image Restoration in interferometrY), implementing methods for the simulation, reconstruction and analysis of Fizeau interferometric images, as well as its application to the case study of the Large Binocular Telescope (LBT). In a third paper (Anconelli et al. 2005) we propose accelerated versions of these methods which allow their use as quick-look methods to be routinely used for data reduction. The quick-look image then can be used to investigate the object and extract information for improved reconstruction. A first example of this two-step approach is given in Correia et al. (2002) where we sketch a possible method for the super-resolved reconstruction of binary systems. In this paper we generalize and validate this method; the implemented algorithms have been inserted in the Software Package AIRY, version 2.0 (see <http://dirac.disi.unige.it> and <http://www.arcetri.astro.it/caos>).

In astronomy and microscopy, super-resolution is a term which, in general, is used to indicate any method able to

improve resolution beyond the diffraction limit. In the case of a telescope with a single mirror of diameter  $D$ , perfect optics and no atmosphere, this limit is approximately given by  $\lambda/D$ , where  $\lambda$  is the wavelength of the observed radiation; in the case of interferometers such as LBT, it is given by  $\lambda/B$ , where  $B$  is the maximum baseline. The idea of overcoming such a limit with a suitable processing of the detected images is an old one and dates back to papers by Toraldo di Francia (1955), Wolter (1961), Harris (1964), McCutchen (1967), Rushforth & Harris (1968) and others.

Resolution beyond the diffraction limit requires the extrapolation of the Fourier transform of the object outside the band of the optical instrument and, as remarked in the papers by Wolter and Harris mentioned above, this is possible if the object has a finite extent. Since the extrapolation problem is ill-posed (in practice, very sensitive to noise propagation from the data to the solution), unlimited super-resolution is impossible in the presence of noise. A first attempt at estimating how much super-resolution can be achieved in practice was developed in Bertero & Pike (1982), where it is shown that the amount of super-resolution is basically controlled by two parameters: the

*space-bandwidth product* (SBP) and the *signal-to-noise* ratio (SNR). In the case of a telescope the SBP is approximately given by the ratio between the angular diameter of the object and the diffraction limit; then the results derived in the paper mentioned above imply that super-resolution is feasible when this parameter is not much greater than one, namely in the case of compact and unresolved objects. On the other hand the amount of super-resolution increases with increasing SNR. An estimate in terms of the photon flux is given by Lucy (1992a,b). A survey of the mathematical foundations of super-resolution is given in Bertero & De Mol (1996) (see also Bertero & Boccacci 1998).

According to the previous remarks, the development of a super-resolving method requires an estimate of the domain  $\mathcal{D}$  of the object, to be used as a constraint in the restoration algorithm so that the total flux of the restored object is concentrated within  $\mathcal{D}$ . In addition, it has been claimed by other authors that other constraints may provide super-resolution. One is non-negativity, which is implemented, for instance, in the maximum entropy method. However, it has been proved that maximum entropy provides super-resolution in the case of the so-called *nearly black objects*, i.e. objects that are zero in the vast majority of the pixels (Donoho et al. 1992). In general, non-negativity works well when combined with the sparsity of the object, as shown by Donoho (1992). It is also known that the restoration of a sparse object is stable with respect to noise if the restoration algorithm implements a constraint on the total flux of the object.

The frequently used RL method (Richardson 1972; Lucy 1974), also known in emission tomography as the Expectation Maximization (EM) method (Shepp & Vardi 1982), implements in a quite natural way both the constraint of non-negativity and that on the total flux of the image. Moreover it implements also the constraint on the domain of the object if a suitable initialization of the iterations is used. The same remarks apply to the OS-EM method (Hudson & Larkin 1994) we have extended to LBT imaging (Bertero & Boccacci 2000a,b). Therefore these methods provide algorithms implementing all the relevant constraints and they appear quite suitable for estimating the amount of super-resolution achievable in practical situations.

In Sect. 2 we introduce the algorithm proposed in this paper and based on RL-like methods. In Sect. 3 we describe the simulation of the PSFs and their correction due to adaptive optics (AO), together with the generation of the simulated images of binary systems. In Sect. 4 we give the results obtained with the proposed algorithm both in the case of a monolithic mirror and in the case of an interferometer such as LBT. Possible applications and perspectives of the method are discussed in Sect. 5.

## 2. The super-resolving algorithm

The proposed super-resolving algorithm is based on the RL method in the monolithic case and on the OS-EM method in the LBT case (the version of these methods, implemented in AIRY, is given in Anconelli et al. 2005). It is a two-steps algorithm, each step consisting of RL or OS-EM iterations. Moreover we

introduce a third step which may be required to estimate the correct photometry of stellar systems such as binaries.

The basic property of the RL and OS-EM methods, which allows their use as super-resolving algorithms, derives from the fact that the result of one iteration contains as a factor the result of the previous one; therefore, if the initial guess is zero at a given pixel, then the result of all the iterations will be zero at that pixel. We call such a property the *localization property* of these methods, in the sense that we can constrain the object to be localized in a given domain  $\mathcal{D}$  by a suitable initialization of the iterations, namely a function which is constant over  $\mathcal{D}$  and zero elsewhere.

Our approach to super-resolution applies to the case where the astronomical target consists of unresolved objects (angular size of the order of the diffraction limit) separated by an angle considerably greater than the diffraction limit (sparsity condition), so that there is no overlapping of their images. For simplicity we assume that there is only one of these unresolved objects, surrounded by empty sky. Then the approach consists of the following steps.

*Step 1* - Apply the RL or OS-EM method to the detected images, using a constant array as initial guess and a number of iterations such that the restored object is sufficiently well localized. If the angular separation is not much smaller than the diffraction limit and the magnitude difference is small, it may happen, in the case of a binary, that the two stars are already resolved in this first step. In such a case one can estimate their positions by computing the centroids and go directly to Step 3 for a more accurate estimate of their magnitudes.

If the two stars are not resolved, then go to Step 2.

*Step 2* - Define the domain  $\mathcal{D}$  of the object by identifying the pixels where the flux of the result of Step 1 is greater than a selected threshold (for instance some percent of its maximum value); alternatively one can take a disc with a diameter equal to the diffraction limit and containing most of the flux of the reconstructed object.

Apply again the RL or OS-EM method to the detected images, but now initialized with the mask of the domain, namely a function which is constant over the domain and zero elsewhere. Each iterate is localized in the selected domain; if, after a number of iterations, the two stars are separated, their positions are obtained by computing their centroids.

To illustrate the method, we show an example of its application in Fig. 1. The parameters used in the simulation are described in Sect. 3. The object, shown in the upper-left panel, consists of two unresolved binaries, the angular separation of each binary being about 1/3 of the diffraction limit while the angular separation of the centres of the two stars is about 2/3 of the diffraction limit. In each binary the difference in magnitude is zero, while the difference in magnitude between the two binaries is 0.5. The images were generated by convolving the object with three ideal LBT PSFs, corresponding to equally spaced parallactic angles ( $0^\circ$ ,  $60^\circ$ , and  $120^\circ$ ), and by perturbing the result with photon and read-out noise. For the first step we selected 1000 OS-EM iterations initialized with a uniform array; the result is shown in the upper-right panel of Fig. 1.

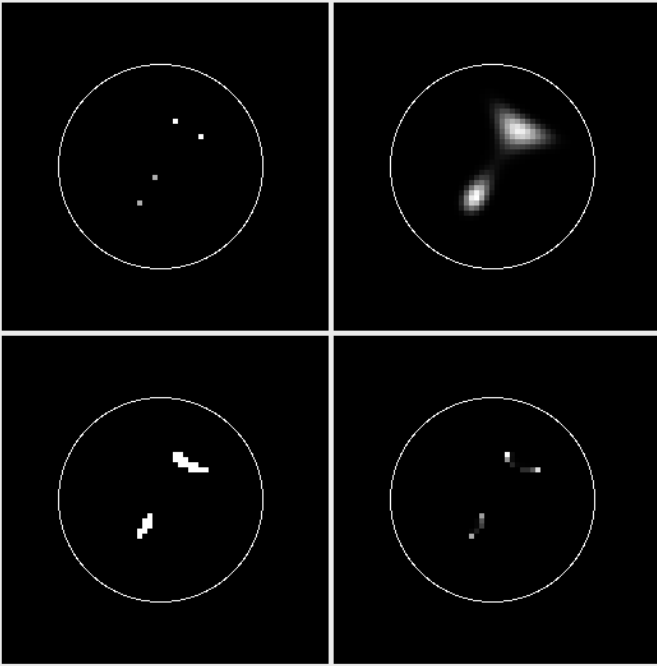


**Fig. 1.** *Upper-left panel:* the object; *upper-right:* the reconstruction after 1000 OS-EM iterations (first step); *lower-left:* the mask obtained with a thresholding of the previous reconstruction (50% of the maximum value); *lower-right:* the restoration after 1000 OS-EM iterations, initialized with the previous mask (second step). The diameter of the circle shown in each picture is  $\lambda/B$ .

The two binaries are resolved but not the stars within each binary. Then a mask was estimated by selecting the pixels where the flux is greater than 50 % of the maximum value of the restored image; the result is shown in the lower-left panel. Finally this mask is used for re-initializing OS-EM and the result is shown in the lower-right panel. The two binaries are clearly resolved. In this case also the magnitudes are obtained with a sufficient accuracy (few percent errors), as the angular separations.

However, in our numerical simulations on binary systems we have verified that, when there is a significant difference of magnitudes between the two stars, these may not be correctly estimated at the end of the second step, while their angular positions are, in general, correctly estimated. In order to overcome this difficulty we propose the following third step.

*Step 3* - Let us assume, in general, that the restored object, provided by Step 1 or Step 2, consists of  $q$  stars localized at the pixels  $P_1, P_2, \dots, P_q$ . We denote by  $\mathbf{K}_j^{(i)}$  ( $j = 1, \dots, p$ ) the PSFs centered at  $P_i$  and given by:

$$\mathbf{K}^{(i)} = \mathbf{K} * \delta(P_i) , \quad (1)$$

where  $\delta(P_i)$  is the characteristic function of the pixel, i.e. it is one at pixel  $P_i$  and zero elsewhere. Then we introduce the images:

$$\mathbf{g}_{j,c} = \sum_{i=1}^q c_i \mathbf{K}_j^{(i)} , \quad (2)$$

depending on the unknown parameters  $c = \{c_1, c_2, \dots, c_q\}$ . These are determined by means of a least-squares method, namely by minimizing the discrepancy:

$$\Delta(c) = \sqrt{\sum_{j=1}^p \|\mathbf{g}_{j,c} - \mathbf{g}_j\|_2^2} , \quad (3)$$

where  $\|\cdot\|_2$  denotes the usual Euclidean norm.

### 3. Image generation

In our numerical simulations we consider the case of LBT both in its “first-light” scheme (one pupil of 8.25 m effective diameter), and in its “second-light” scheme (two pupils separated by 14.4 m and recombined interferometrically in a Fizeau way). The first scheme implies the simulation of the first-light AO system of LBT (Esposito et al. 2003), while the second scheme is to be considered within the framework of the LINC-NIRVANA instrument (Ragazzoni et al. 2003; Herbits et al. 2003). The main features of both systems are the use of pyramid wavefront sensors and the LBT 672 adaptive secondary mirror (Riccardi et al. 2003).

The tool employed for numerically simulating the PSFs relative to the two cases is the Software Package CAOS (Carbillet et al. 2004) which is used to simulate in detail the whole process of atmospheric propagation of light, wavefront sensing (with a complete model of the pyramid wavefront sensor), wavefront reconstruction (using the LBT 672 adaptive secondary mirror modes), and dynamic closing of the loop. In the case of the interferometric PSFs, the Fizeau recombination of light, together with the related differential piston error, is also taken into account.

#### 3.1. The AO-corrected PSFs

A detailed explanation of the method and of the tuning of the system parameters for the simulation of our AO-corrected monolithic (one pupil) PSFs can be found in Carbillet et al. (2003). We will here only briefly recall the main physical parameters considered for the present case. The multi-layer atmosphere has an average layer velocity of 15 m/s, a total Fried parameter  $r_0$  (@500 nm) = 0.15 cm, a wavefront outer scale  $\mathcal{L}_0 = 20$  m, and a resulting seeing of roughly 0.5". The guide star considered has an *R*-band magnitude of 13 and is a K5 spectral type. The sensing band is 600–900 nm (roughly *R* and the first part of *I*) and the average total transmission related to the sensing is approximately of 40%. Following Carbillet et al. (2003) the optimum sensor configuration is therefore the one corresponding to 15×15 sub-apertures, with an exposure time of 1.67 ms, and 150 LBT 672 modes reconstructed.

Figure 2 shows the resulting *K*-band PSFs, compared with the ideal one that would be obtained in case of no perturbations at all from the atmosphere. The on-axis PSF has a Strehl ratio of ~79%, while the off-axis PSF is at 15" away from it, with a resulting Strehl ratio of ~67%. Note that the difference in Strehl ratio between the two PSFs is highly dependent on the turbulent layers distribution (the higher the turbulence, the

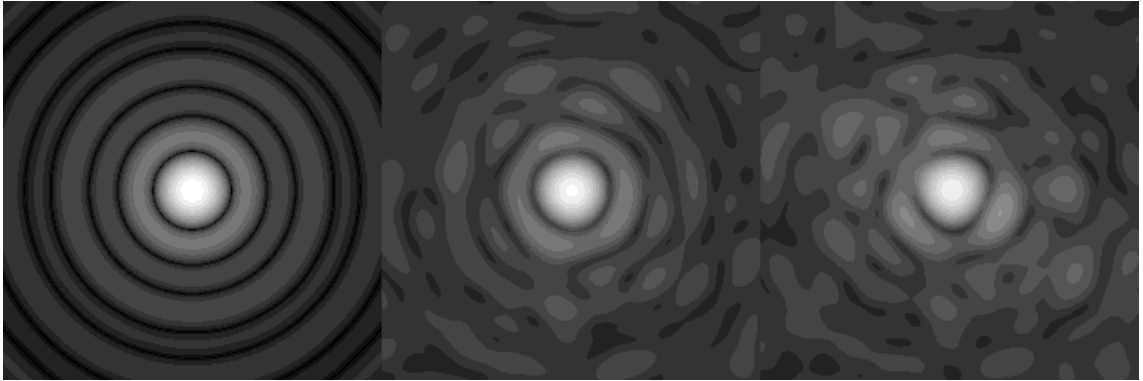


**Fig. 2.** One-pupil AO-corrected  $K$ -band PSFs: ideal case (*left*), on-axis case (*middle*), and  $15''$  off-axis case (*right*). The total field is  $256 \times 0.0025 = 0.64''$  and for rendering purpose the images are shown at the power of 0.2. Note the slight difference in image quality between the on-axis PSF and the off-axis PSF.

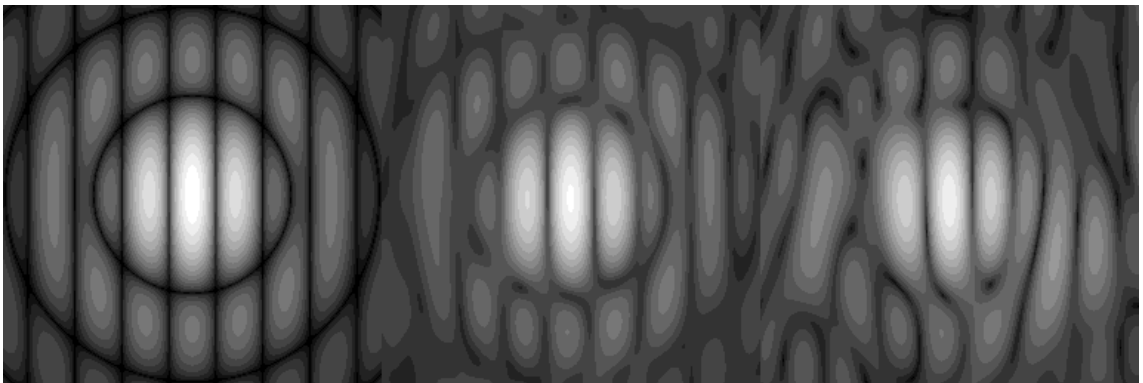


**Fig. 3.** Interferometric AO-corrected  $K$ -band PSFs: ideal case (*left*), on-axis case (*middle*), and  $15''$  off-axis case (*right*). The total field is  $256 \times 0.001 = 0.256''$  and for rendering purpose the images are shown at the power of 0.2. The difference in image quality between the on-axis PSF and the off-axis PSF is appreciable. The PSFs shown here correspond to the case of  $0^\circ$  parallactic angle. Note that in our simulations we use two other similar sets at  $60^\circ$  and  $120^\circ$ .

lower the off-axis Strehl ratio). Moreover we assume the optimistic case where a reference star is available in the vicinity of the observed object. This may depend on the detector size. In principle we require a very large detector because we assume that we have a pixel size of 2.5 mas, which is a considerable over-sampling: since the diffraction limit is about 50 mas (the considered band is  $K$ , 2200 nm), we have approximately  $20 \times 20$  pixels within a resolution element. However, as we discuss in Sect. 5, the required oversampling can be obtained by a rebinning of the detected images if these are moderately over-sampled, as it will be in the case of LBT.

Starting from the known performance of the first-light AO system of LBT (monolithic case explained above), and assuming that at least the single-conjugate phase of LINC-NIRVANA will have a similar behaviour, the resulting set of interferometric images is then composed from observations at different parallactic angles (here  $0^\circ$ ,  $60^\circ$ , and  $120^\circ$ ), corresponding to three different moments during the observation night, and therefore to three different realizations of the turbulent atmosphere. The AO system behaviour is simulated with the same sets of parameters as for the monolithic case, but with the additional effect of a differential piston residual. The pixel size is 1 mas (again about  $20 \times 20$  pixels within a resolution element, since the diffraction limit is about 20 mas in  $K$ -band). The

resulting Strehl ratio of the on-axis PSF is  $\sim 77\%$  (averaged over the 3 realizations), while that of the off-axis one ( $15''$ ) is  $\sim 66\%$ . Figure 3 shows the resulting interferometric PSFs corresponding to a  $0^\circ$  parallactic angle.

### 3.2. Image formation

Sets of binary star images are formed starting from the sum of two shifted PSFs (see Eq. (1)), centered on the pixels of the two stars, and weighted with the desired magnitudes. Sky background emission is then added and the resulting images are eventually corrupted with Poisson and detector noise. The overall efficiency taken into account for both the monolithic 8 m PSFs and the interferometric PSFs is 30%.  $K$ -band sky background is  $12.5 \text{ mag/arcsec}^2$ , read-out noise is  $2 e^- \text{ rms}$ , and dark current noise is neglected. The integration time considered in both cases is 20 min, and the  $K$ -band magnitudes considered (concerning the binary main component) range from 10 to 17. In such a situation we can consider the images as dominated by photon noise, so that the signal-to-noise ratio (SNR) simply depends on the square root of the number of object photons. As a consequence the interferometric case shows a SNR improvement by a factor of  $\sim \sqrt{6}$  with respect to the monolithic case, since we are considering two 8m pupils and three different

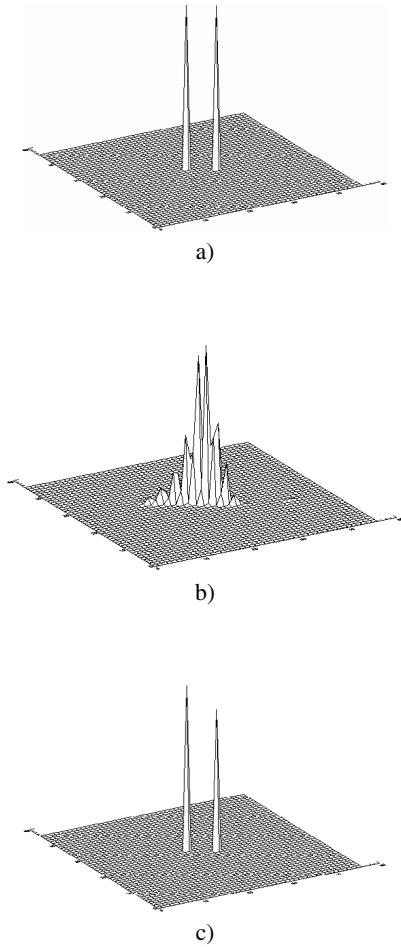


**Fig. 4.** Example of application of the two-step algorithm. The object is a binary consisting of two stars with angular separation  $\frac{1}{4}\lambda/B$  ( $B$  = maximum baseline of LBT) and with the same magnitude  $m = 12$ ; three interferometric noisy images are generated by convolving the object with the PSFs with an average Strehl ratio of 66% and are deconvolved by means of the PSFs with an average Strehl ratio of 77% (see Fig. 3): a) the original object; b) the restored object obtained after Step 1; c) the restored object obtained after Step 2.

parallactic angles. Such an improvement corresponds to roughly 1 mag gain.

## 4. Numerical results

In this section we validate the super-resolving algorithm proposed in this paper by considering the problem of estimating the astrometric and photometric parameters of unresolved binary systems. We consider first the case of a single mirror and next the interferometric case. We estimate the performance of the algorithm both when the ideal PSF is used for convolving and deconvolving the binary (this simulation provides the maximum attainable super-resolution for the given SNR) and when different AO-corrected PSFs are used for convolution and deconvolution.

After an analysis of a few cases, we decided to use 10 000 RL-iterations in Step 1 and up to 5000 RL-iterations in Step 2; indeed, in Step 2, the number of iterations depends on the result of Step 1 and, in some lucky cases can be small

(about 250). In general the analysis of each single case can be quite heavy from the computational point of view, especially in the interferometric case (about a factor of 3 in computation time with respect to the monolithic case). In Fig. 4 we give a typical result of the two-step algorithm together with the original object. The parameters characterizing the numerical experiment are given in the caption. In this case Step 3 is not required.

### 4.1. The monolithic case

The super-resolution attainable for given values of the observational parameters (efficiency, integration time, etc.) depends both on the magnitude of the primary star and on the magnitude difference between the two stars. Since a complete analysis should require the investigation of a very large number of possible cases, we introduce a number of limitations in the choice of the parameters.

The first study concerns the limit attainable in angular separation by assuming that the magnitude difference between the two stars is zero and that the  $K$ -band magnitude of the single component ranges from 10 to 17. For each of these values we search for the minimum binary separation allowing for detection and characterization of the system.

The second study concerns the limit attainable in the magnitude difference  $\Delta m$  between the two stars by fixing their angular separation to  $\frac{1}{2}\lambda/D$  (we think that this is a relevant value in the potential applications of the method); moreover, as above, we assume that the magnitude of the primary component ranges from 10 to 17. Again, for each value of the primary magnitude we search for the maximum magnitude difference allowing detection and characterization of the system.

We consider three different cases, denoted as **A**, **B**, and **C**. In case **A** ideal PSFs are used both for convolution (image formation) and deconvolution. Case **B** and case **C** concern AO-corrected PSFs. In case **B** the observed object (the unresolved binary system) is also used as the AO guide star while the image of an off-axis point-like reference star is used as the PSF for deconvolution. This is probably the most common case. We also consider the case where the image of the AO guide star is used for deconvolving the binary image (case **C**), i. e. the role of the two PSFs is exchanged with respect to case **B**; such a situation is realistic when the observed object is fainter than the reference star in the wavefront sensing band.

#### 4.1.1. Binary separation limit

As stated above, in this simulation study we assume  $\Delta m = 0$  and we fix to 10 000 the number of iterations of Step 1; the number of iterations of Step 2 ranges from 250 to 5000 (iterations are pushed until clear separation of the binary components is detected). In cases **A** and **B** the mask used in Step 2 is based on an intensity thresholding of the image reconstructed in Step 1, while in case **C** we apply a circular mask of diameter  $\leq \lambda/D$ . This mask suppresses artifacts which may appear outside the region of interest (ROI), namely a region with a size of the order of the resolution limit  $\lambda/D$ . We point out that, since in all these cases we have  $\Delta m = 0$ , the first two steps provide

**Table 1.** Summary of the results obtained in the case where the magnitude difference between the two stars is zero – monolithic case. Sep. is the minimum separation, in units of  $\lambda/D$ , allowing for detection and characterization of the binary system.

Main star <i>K</i> -band mag.	Case <b>A</b> Sep. [ $\lambda/D$ ]	Case <b>B</b> Sep. [ $\lambda/D$ ]	Case <b>C</b> Sep. [ $\lambda/D$ ]
10	3/20	1/4	1/4
11	3/20	1/4	3/10
12	3/20	3/10	3/10
13	3/20	3/10	3/10
14	3/20	3/10	3/10
15	3/20	3/10	3/10
16	1/4	3/10	3/10
17	1/4	3/5	3/10

both the angular positions and the magnitudes with sufficient accuracy and Step 3 is not required.

For the search of the minimum separation which can be resolved, we consider angular separations which are integer multiples of the pixel size, so that we have an accuracy of about one pixel. Since, as indicated in Sect. 3, we have 20 pixels within a resolution element  $\lambda/D$ , our accuracy is about  $\lambda/20D$ . Our results are summarized in Table 1.

As follows from this table, the amount of super-resolution obtained in the ideal case is spectacular but the effect is greatly reduced by incomplete AO correction, even if rather high AO corrections are considered in our simulations. Moreover, as is expected, the effect decreases for increasing magnitudes, because the SNR is decreasing. We also point out that the difference between the super-resolution attainable in case **B** and that attainable in case **C** is about one pixel and therefore these two cases can be considered as equivalent within our accuracy. This result is reasonable because, as follows from Fig. 1, the difference between the two PSFs used in these simulations is not very relevant. A gain of a factor of 4 in resolution, as estimated in both cases for the brightest binaries, can be considered as remarkable.

#### 4.1.2. Magnitude difference limit

In this study Step 2 is not necessary in cases **A** and **B**, except for the fainter magnitude (17), while it is always necessary in case **C** in order to eliminate artefacts outside the ROI. In all cases the magnitudes must be estimated by means of Step 3. In order to reduce computation time we have considered steps of 0.5 mag in the variation of the magnitude difference between the two stars.

Our results are summarized in Table 2 where the following notations are used:

- $\Delta m_0$  = maximum magnitude difference which can be detected;
- $\Delta \Theta_r$  = relative reconstruction error on the angular separation;
- $\Delta m_r$  = reconstructed magnitude difference.

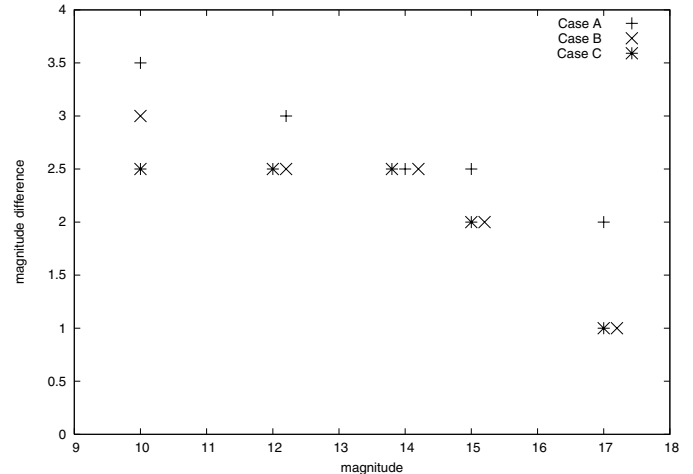


**Fig. 5.** Behaviour of the maximum magnitude difference  $\Delta m_0$  which can be detected as a function of the magnitude  $m$  of the main component – monolithic case. For the sake of clarity coincident points are represented with a small horizontal shift.

Moreover in Fig. 5 we plot the behaviour of the magnitude difference limit as a function of the magnitude of the main component, in the three different cases.

Again the best results are obtained in the ideal case, even if the difference between the three cases is not as significant as in the previous study concerning angular separation. The reason probably is that, in this study, we only require an improvement in resolution by a factor of 2. The maximum difference in magnitude attainable decreases with increasing values of the primary magnitude, namely with decreasing SNR. Similarly, the error in estimating the magnitude difference (i.e. the difference between  $\Delta m_0$  and  $\Delta m_r$ ) increases with decreasing SNR.

The magnitude difference is around 3 for the brightest cases and is  $\sim 1$  even in the case of a binary with a 17th main component magnitude (hence corresponding to a binary star combined magnitude of  $\sim 16.6$ ).

#### 4.2. The interferometric case

In the interferometric case, we follow the same simulation strategy introduced in the monolithic case. We investigate the minimum separation attainable in the case where  $\Delta m = 0$  and the maximum difference magnitude attainable in the case where the angular separation is  $\frac{1}{2}\lambda/B$ ,  $B$  now being the maximum baseline of LBT. Again we consider three cases: **A**, **B**, and **C**. In case **A** ideal interferometric PSFs are used both for convolution (image formation) and deconvolution. In case **B** the observed object (the unresolved binary system) is also used as the AO guide star and therefore images are obtained by convolving the object with the PSFs corresponding to a Strehl ratio of about 77% while the PSFs corresponding to a Strehl ratio of about 66% are used for deconvolution (see Fig. 3). In case **C** the role of the two sets of PSFs is exchanged.

**Table 2.** Summary of the results obtained in the case where the angular separation of the two stars is  $\frac{1}{2}\lambda/D$ . The quantities  $\Delta m_0$ ,  $\Delta\Theta_r$ , and  $\Delta m_r$  are defined in the text.

main star <i>K</i> -band mag.	case <b>A</b>			case <b>B</b>			case <b>C</b>		
	$\Delta m_0$	$\Delta\Theta_r$	$\Delta m_r$	$\Delta m_0$	$\Delta\Theta_r$	$\Delta m_r$	$\Delta m_0$	$\Delta\Theta_r$	$\Delta m_r$
10	3.5	20%	3.75	3	20%	2.8	2.5	20%	2.4
12	3	10%	3.2	2.5	20%	2.5	2.5	15%	3.3
14	2.5	20%	2.5	2.5	20%	2.2	2.5	15%	3.1
15	2.5	20%	2	2	10%	1.5	2	20%	2.7
17	2	20%	1	1	20%	0.4	1	10%	0.4

**Table 3.** Summary of the results obtained in the case where the magnitude difference between the two stars is zero – interferometric case. Sep. is the minimum separation obtained in units of  $\lambda/B$ , where  $B$  is the maximum baseline of LBT.

main star <i>K</i> -band mag.	Case <b>A</b> Sep. [ $\lambda/B$ ]	Case <b>B</b> Sep. [ $\lambda/B$ ]	Case <b>C</b> Sep. [ $\lambda/B$ ]
10	3/20	3/20	3/20
11	3/20	3/20	1/5
12	3/20	3/20	1/4
13	3/20	3/20	1/4
14	3/20	1/4	1/4
15	3/20	1/4	1/4
16	1/5	1/4	1/4
17	1/5	1/4	1/4

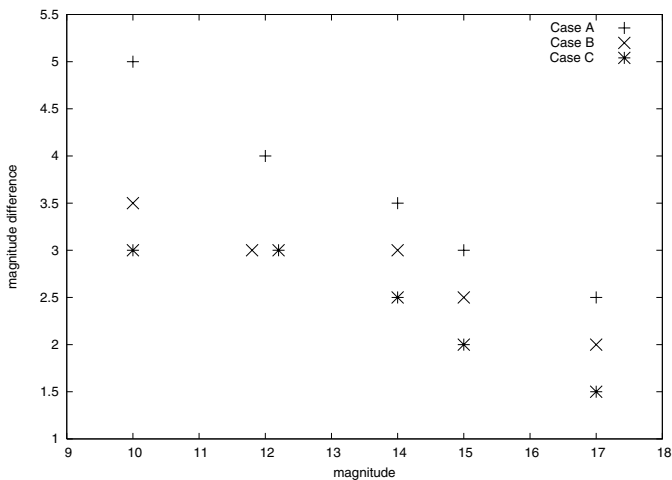


**Fig. 6.** Behaviour of the maximum magnitude difference limit  $\Delta m$  which can be detected as a function of the magnitude  $m$  of the main component – interferometric case. For the sake of clarity coincident points are represented with a small horizontal shift.

#### 4.2.1. Binary separation limit

As in the monolithic case we perform 10 000 iterations in Step 1 while the iterations of Step 2 are pushed until clear separation of the two stars is obtained. Again Step 3 is not required and we consider angular separations which are integer multiples of the pixel size. Therefore our accuracy is about  $\lambda/20B$ . Our numerical results are summarized in Table 3.

These results look even better than those obtained in the monolithic case, but one must take into account that each image of LBT has a higher SNR than the image of the monolithic case (roughly a factor  $\sqrt{2}$ ) and that we use three images

corresponding to different baselines (see the comment at the end of Sect. 3). The effect of this higher SNR will be reconsidered in connection with the subsequent results. At least for the brightest binaries, the amount of super-resolution does not strongly depend on the amount of AO correction and is considerable. As it is obvious, an improvement in resolution by a factor of about 7 in the case  $m = 10$  is quite surprising; even if it will not be attained in real observations, it indicates that LBT can be compatible with a remarkable amount of super-resolution. This will probably depend also on the orientation of the binary axis with respect to the observation baselines, as can be expected from the angular coverage study we made in Carillet et al. (2002).

Here one can appreciate the difference between the two AO-corrected cases, namely **B** and **C**. Such a difference (case **B** permits a higher amount of super-resolution for medium-high binary magnitude cases) can be reasonably explained by the fact that in case **B** the images correspond to PSFs with a higher AO correction and therefore intrinsically contain more information than those of case **C**. As also follows from Fig. 2, the difference between the two PSFs is much more significant than that observed in the monolithic case.

To be very conservative we can conclude that a gain of a factor 5 in resolution is clearly attainable in the brightest cases.

#### 4.2.2. Magnitude difference limit

In this simulation study the angular separation is fixed, as indicated above. Moreover we use the same notations introduced in the monolithic case for the maximum magnitude difference, the error on angular separation and the reconstructed magnitude difference. Our numerical results are summarized in Table 4. Moreover in Fig. 6 we plot the behaviour of the magnitude difference limit as a function of the magnitude of the main component, for the three cases we have considered.

Again we find better results than those obtained in the monolithic case. However, if we compare the two tables, we find that in the interferometric case we have an improvement of about one order of magnitude with respect to the monolithic case and such an improvement is compatible with the higher SNR of the interferometric images as discussed at the end of Sect. 3.

## 5. Discussion

In this paper we have proposed an algorithm for the super-resolution of stellar systems, with an application to binary stars.

**Table 4.** Summary of the results obtained in the case where the angular separation of the two stars is  $\frac{1}{2}\lambda/B$ , where  $B$  is the maximum baseline of LBT.

main star <i>K</i> -band mag.	case A			case B			case C		
	$\Delta m_0$	$\Delta\Theta_r$	$\Delta m_r$	$\Delta m_0$	$\Delta\Theta_r$	$\Delta m_r$	$\Delta m_0$	$\Delta\Theta_r$	$\Delta m_r$
10	5	20%	3.5	3.5	20%	2	3	22%	2.5
12	4	10%	2.8	3	20%	2	3	22%	2.5
14	3.5	10%	2.5	3	20%	1.8	2.5	22%	2.3
15	3	10%	2.3	2.5	10%	1.7	2.5	22%	2
17	2.5	10%	1.7	2	0%	1.4	1.5	10%	1

From a general point of view we have shown that the well-known RL algorithm can be used for such a purpose if it is joined with a suitable initialization of the iterations, namely the mask of the domain where the unresolved object is localized.

We have shown that, in case of relatively high SNR (small magnitudes) and relatively high AO correction, a gain of a factor from 4 to 5 in resolution is clearly attainable. This would make similar the results from an 8 m telescope, equipped with a high-order AO system and our deconvolution method, to a 30 m future telescope, rescaling at least the object magnitude because of the obvious differences. In an equivalent manner, this would also allow comparison of a telescope such as LBT in its interferometric mode to a 100 m Extremely Large Telescope (ELT), or, more reasonably, to the VLTI with two Unit Telescopes (UT) and a baseline of  $\sim 50$  m, considering that the limit in resolution for a Michelson interferometer is typically  $\lambda/2B$ .

However this remark does not mean that we propose Fizeau interferometers as competitors to the Michelson ones for the analysis of, for instance, binary systems. We only mean that an astronomer observing with LBT, hence with a wide field of view ( $10''$  in the case of the detector of the beam combiner LINC-NIRVANA), has a method for investigating whether an unresolved stellar object in the field has a structure or not and for attempting a quantitative analysis.

The crucial point in our approach is that it needs an oversampling of the data which is not provided by the existing detectors. However, a moderate oversampling will be available with the detectors designed for the first light of LBT and for LINC-NIRVANA, as discussed below. Therefore we performed a numerical experiment in order to verify that the required oversampling can be obtained by a suitable rebinning of the images. The experiment applies to the object of Fig. 1 and consists of the following steps:

- three LBT images, with a sampling distance of 1 mas, are generated by convolving the object with ideal PSFs corresponding to  $0^\circ$ ,  $60^\circ$ , and  $120^\circ$ ;
- the three images are rebinned to 5.12 mas (the sampling distance of the detector of LINC-NIRVANA in *K* band) and then are perturbed with photon and read-out noise;
- the noisy images are now re-rebinned to 1 mas;
- these final images are deconvolved with ideal PSFs.

In the third step the cubic interpolation provided by the standard IDL routine *congrid* is used but, of course, more refined interpolation methods could be devised.

The experiment was successful, in the sense that the two binaries were resolved and the accuracy in the estimation of the astrometric and photometric parameters was still satisfactory. For instance we have a few percent increase of the errors in the estimation of the angular separations; as concerns the magnitude difference between the two binaries, we find 0.49 in the experiment of Fig. 1 and 0.4 in the rebinning experiment, the correct value being 0.5. Of course our simulation does not correspond exactly to the real detected images, but it is promising and therefore we think that a rebinning strategy is a viable approach in practice.

As an alternative to a numerical rebinning, one could also consider dithering the data (see e.g. Fruchter & Hook 2001), although it can be objected that this is probably not necessary since it does not add information if the images are already sampled well beyond the Nyquist limit. The super-resolution capabilities come from the fact that the deconvolution algorithm tries to extrapolate information down to the pixel limit, hence a numerical rebinning is probably sufficient. A study of these two techniques, possibly combined to obtain over-sampled data is beyond the scope of this paper but will soon be the object of further study.

The results we have derived in the monolithic case could be applied to observations with the first-light AO system of LBT together with the near-infrared instrument LUCIFER (Mandel et al. 2001). Since the pixel size of this instrument is 15 mas in *J*, *H*, *K* band and since the resolution is 55 mas in *K* band, we see that the conditions for applying the rebinning procedure outlined above are satisfied. The same remark applies to interferometric observations with LINC-NIRVANA in its single-conjugated AO configuration, since the pixel size will be 5.12 mas in *J*, *H*, *K* band, with a resolution of 20 mas in *K* band.

Another important problem is the PSFs determination, i. e. the obtention of a suitable reference star for the PSF estimation and subsequent deconvolution of the scientific images. This problem could in some cases lower the performances evoked in this paper. Nevertheless, if a suitable star is not present in the field of view of the detector, this problem could be addressed by changing the pointing of the telescope in a reasonable time, as is done routinely in speckle imaging (see, for instance, Carbillet et al. 1996; Aristidi et al. 1997) to take images of point-like sources.

A last crucial point in our approach is the choice of the mask, which is fundamental for obtaining a good reconstruction. In the module DEC of the software package AIRY, where we have implemented our approach, we allow three possible

choices: a circular mask with diameter equal to the resolution limit of the telescope; a mask defined by a thresholding of the image reconstructed in Step 1, the threshold being selected by the user, and a user-defined mask. The first mask is useful when artifacts, clearly due to noise amplification, are present outside the region of interest while the second one requires the choice of the threshold. No precise rule can be given for this but, in general, one must look for a threshold between 30 and 50% of the maximum value of the reconstructed image.

*Acknowledgements.* We wish to thank Serge Correia for fruitful interaction and early work on this super-resolution algorithm, and Piero Salinari for useful discussions on this topic in the framework of the LBT telescope.

## References

- Anconelli, B., Bertero, M., Boccacci, P., Carbillet, M., & Lanteri, H. 2005, *A&A*, 430, 731
- Aristidi, É., Carbillet, M., Prieur, J.-P., et al. 1997, *A&AS*, 126, 555
- Bertero M., & Boccacci, P. 1998, *Introduction to Inverse Problems in Imaging* (Bristol: IOP Publishing)
- Bertero, M., & Boccacci, P. 2000a, *A&AS*, 144, 181
- Bertero, M., & Boccacci, P. 2000b, *A&AS*, 147, 323
- Bertero, M., & De Mol, C. 1996, in *Progress in Optics* 36, ed. E. Wolf, 129
- Bertero, M., & Pike, E. R. 1982, *Optica Acta*, 29, 727
- Carbillet, M., Ricort, G., Aime, C., & Perrier, Ch. 1997, *A&A*, 310, 508
- Carbillet, M., Correia, S., Boccacci, P., & Bertero, M. 2002, *A&A*, 387, 744
- Carbillet, M., Vérinaud, C., Esposito, S., et al. 2003, in *Proc. SPIE* 4839, ed. P. L. Winizowitch, & D. Bonaccini, 131
- Carbillet, M., Vérinaud, C., Femenía, B., et al. 2004, *MNRAS*, in press
- Correia, S., Carbillet, M., Boccacci, P., Bertero, M., & Fini, L. 2002, *A&A*, 387, 733
- Donoho, D. L. 1992, *SIAM J. Math. Anal.*, 23, 1309
- Donoho, D. L., Johnstone, I. M., Hoch, J. C., & Stern, A. S. 1992, *J. R. Statist. Soc.*, B54, 41
- Esposito, S., Tozzi, A., Feruzzi, D., et al. 2003, in *Proc. SPIE* 4839, ed. P. L. Winizowitch, & D. Bonaccini, 164
- Fruchter, A. S., & Hook, R. N. 2001, <http://xxx.lanl.gov/abs/astro-ph/9808087>
- Harris, J. L. 1964, *J. Opt. Soc. Am.*, 54, 931
- Herbts, T. M., Andersen, D., Bizenberger, P., et al. 2003, in *Proc. SPIE* 4838, ed. W. A. Traub, 456
- Hudson, H. M., & Larkin, R. S. 1994, *IEEE Trans. Med. Im.*, 13, 601
- Lucy, L. B. 1974, *AJ*, 79, 745
- Lucy, L. B. 1992a, *A&A*, 261, 706
- Lucy, L. B. 1992b, *AJ*, 104, 1260
- Mandel, H., Appenzeller, I., Bomans, D., et al. 2001, in *Proc. SPIE* 4008, ed. M. Iye, & A. F. Moorwood, 767
- McCutchen, C. W. 1967, *J. Opt. Soc. Am.*, 57, 1190
- Ragazzoni, R., Herbst, T., Andersen, D., et al. 2003, in *Proc. SPIE* 4839, ed. P. L. Winizowitch, & D. Bonaccini, 536
- Riccardi, A., Brusa, G., Salinari, P., et al. 2003, in *Proc. SPIE* 4839, ed. P. L. Winizowitch, & D. Bonaccini, 721
- Richardson, W. H. 1972, *J. Opt. Soc. Am.*, 62, 55
- Rushforth, C. K., & Harris, R. W. 1968, *J. Opt. Soc. Am.*, 58, 539
- Shepp, L. A., & Vardi, Y. 1982, *IEEE Trans. Med. Im.*, 1, 113
- Toraldo di Francia, G. 1955, *J. Opt. Soc. Am.*, 45, 497
- Wolter, H. 1961, in *Progress in Optics* 1, ed. E. Wolf, 155